Characterization of porous fluorohydroxyapatite bone-scaffolds fabricated using freeze casting

Tony J. Yin [a], Sujee Jeyapalina [b,c], Steven E. Naleway [a,*]

[a] *Department of Mechanical Engineering, University of Utah, USA*
[b] *Division of Plastic Surgery, Department of Surgery, University of Utah Health, USA*
[c] *Research, Department of Veterans Affairs Salt Lake City Health Care System, USA*

ARTICLE INFO

ABSTRACT:

With the increasing demand for orthopedic and dental reconstruction surgeries, there comes a shortage of viable bone substitutes. This study was therefore designed to assess the efficacy of porous fluorohydroxyapatite (FHA) as a potential bone substitute. For this, porous FHA scaffolds were fabricated using the freeze casting technique. They were then sintered at 1250, 1350 and, 1450 °C, and microstructural, mechanical, and *in vitro* properties were analyzed. The microstructure analyses revealed the porosity remained constant within the temperature range. However, the pore size decreased with increasing sintering temperature. The greatest compressive strength and elastic modulus were obtained at 1450 °C, which were 13.5 ± 4.0 MPa and 379 ± 182 MPa, respectively. These are comparable values to human trabecular bone and other porous scaffolds made using hydroxyapatite. This analysis has thus helped to attain an understanding of the mechanical and material properties of freeze-cast FHA scaffolds that have not been presented before. *In vitro* studies revealed an increasing rate of human osteoblast cell proliferation on freeze-cast FHA scaffolds with increasing sintering temperature, suggesting improved osteogenic properties. Additionally, osteoblasts cells were also shown to proliferate into the interior pores of all freeze-cast FHA scaffolds. These results indicate the potential of porous FHA scaffolds fabricated using the freeze-casting technique to be utilized clinically as bone substitutes.

1. Introduction

Calcium phosphates are used in dental and orthopedic surgeries because of their mechanical properties, corrosion resistance, and biocompatibility (Ramay and Zhang, 2004; Hench, 1998; Sopyan and Gunawan, 2013; Thrivikraman et al., 2017). Among these phosphates, hydroxyapatite (HA) is commonly used because of its stochiometric similarity to the mineral component in bone and for its osteoconductive properties (Dutta et al., 2015). This apatite has been used in multiple ways, which include coatings for titanium implants (Dutta et al., 2015; Dehghanghadikolaei and Fotovvati, 2019; Diez et al., 2016), bone cements for fixation (Alge et al., 2009; Rabiee et al., 2010; Kang et al., 2018), and artificial scaffolds to promote bone growth (Zamanian et al., 2013; Bienek and Skrtic, 2017; Habraken et al., 2007; Milovac et al., 2014). The development of artificial bone scaffolds is necessary because of allograft and autograft shortages due to limited donor availability, prolonged surgery times, and pain (Baldwin et al., 2019; Arrington et al., 1996; Belthur et al., 2008; Russell and Block, 2000; Tuchman et al.,

2016; Boyce et al., 1999; van de Vijfeijken et al., 2018). However, current artificial bone scaffolds often lack the osteoinductive or osteogenic properties and mechanical strength required for long-term bone remodeling and regeneration (Luo et al., 2018; Nuss and von Rechenberg, 2008). As such, there is a need to develop a suitable artificial bone scaffold to improve reconstructive surgery.

Porous bioceramics have been investigated to find an alternative to current bone scaffolds (Sopyan and Gunawan, 2013; Munch et al., 2008; Deville, 2010). The porosity of these porous bioceramics provides a suitable biocompatible environment for cell growth and proliferation (Polo-Corrales et al., 2014). A high porosity also facilitates nutrient and fluid transport (Polo-Corrales et al., 2014). However, porosity generally reduces the mechanical strength and resilience, which is necessary for physiological load bearing (Deville, 2010; Fu et al., 2008a). Multiple methods have been developed to fabricate porous bioceramics, such as polymer replication (Jo et al., 2009; Kim et al., 2009), solid freeform fabrication (Kim et al., 2011), rapid prototyping (Deisinger et al., 2008; Wilson et al., 2004), and freeze casting (Lee et al., 2007, 2017; Deville

---

* Corresponding author.
E-mail address: steven.naleway@mech.utah.edu (S.E. Naleway).

et al., 2006a; Fu et al., 2008b). Notable amongst these is freeze casting, which is a simple and effective technique that allows for tailored porosity, pore structure, and mechanical properties (Nelson et al., 2020; Yook et al., 2012).

The freeze-casting process consists of four steps: (1) a colloidal slurry is mixed using solid loading particles, a freezing solvent, polymeric binders, and a dispersant; (2) the slurry is directionally frozen to segregate the solid particles between the growing ice crystals forming a preliminary scaffold; (3) the frozen scaffold is sublimated at low temperature and pressure to remove the ice crystals resulting in a weak green body; (4) the green body is sintered to fuse the solid particles together while disintegrating the polymeric binders and dispersants with the resultant porous structure of the scaffold being a rough negative of the sublimated ice crystals (Munch et al., 2008, 2009; Nelson et al., 2019a, 2020; Deville et al., 2006b, 2007). While water is a commonly used solvent, other solvents such as camphene (Lee et al., 2007; Han et al., 2010) and tert-butyl alcohol (TBA) (Lee et al., 2019; Tang et al., 2016) have also been used. Camphene is notable because it maintains a solid state in ambient conditions and can produce highly dendritic crystal growth during freezing (Lee et al., 2007; Han et al., 2010). Alternatively, tert-butyl alcohol produces a variety of crystal structures based on the TBA content during freezing, with a hexagonal pore structure obtained with pure TBA (Lee et al., 2019). The freeze-casting process is based on physical particle interactions with the freezing solvent, so the process can be achieved independently of the material's chemistry (Deville, 2010; Deville et al., 2006a, 2006b). As a result, HA structures made through freeze casting have shown promise as bone-scaffolds, with mechanical strengths and porosities similar to what is seen in trabecular bones (Zamanian et al., 2013; Fu et al., 2008a; Deville et al., 2006a).

HA has been used in multiple biomedical applications as HA-based or composite materials such as coatings (Diez et al., 2016; Kim et al., 2004; Bai et al., 2019), bone cements (Rabiee et al., 2010; Kang et al., 2018), and artificial implants (Sopyan and Gunawan, 2013; Gaviria et al., 2014). The material has osteoconductive properties and elicits a limited immune response (Ghanaati et al., 2010, 2012; Al-Maawi et al., 2017). Over the past decade, multiple scaffolds using HA and other calcium apatites have been developed (Kattimani et al., 2016). Despite the focus, limitations still remain when using the material. When HA is sintered above 850 °C to increase the mechanical strength, the HA begins to decompose into other calcium phosphates, resulting in a weaker structure and highly resorbable forms, which results in poor biocompatibility (Ou et al., 2013; Ghazanfari and Zamanian, 2013). Stoichiometrically altering the HA by partially replacing the hydroxyl group with fluorine yields fluorohydroxyapatite (FHA), which resolves the previous issues. Studies on FHA have shown enhanced biocompatibility when compared to HA (Liu et al., 2019; Rojaee et al., 2014). Studies on the effects of temperature also show that FHA has higher thermal stability in comparison to HA by limiting the decomposition into tricalcium phosphate (TCP) (Zhao et al., 2010; Chen et al., 2015). TCP scaffolds show a higher resorption rate compared to HA and FHA, but if the quantity is controlled, TCP can also be used to tailor the resorption rate (Ghanaati et al., 2012; Chu et al., 2013). Improved mechanical properties are also expected to come with improved thermal stability. Kim et al. (2004) demonstrated increased mechanical properties in zirconia composites with HA and FHA, with flexural strength, fracture toughness, and hardness improving with increasing fluoride composition.

To date, multiple studies have examined the use of FHA composites in the development of biomedical applications (Kim et al., 2004; Bai et al., 2019; Rojaee et al., 2014; Fathi and Mohammadi Zahrani, 2009). However, little research has focused on pure porous FHA scaffolds. In this study, an understanding of the mechanical and material properties of freeze-cast FHA scaffolds was established. Scaffolds were sintered at 1250 °C, 1350 °C, and 1450 °C to determine the effects of sintering on thermal stability and mechanical properties. The scaffolds and their resulting properties were evaluated on their similarities to human bone.

Additionally, an assay using the MTT (tetrazolium salt) kit was conducted to evaluate osteoconduction *in vitro*. These results demonstrated that freeze-cast FHA scaffolds showed potential as biomedical implants.

2. Materials and methods

2.1. Apatite synthesis

Apatite powders were synthesized in-house. FHA was prepared using a published methodology, which was described fully in our previous paper (Bennett et al., 2019). The fluoridated apatites, FHA, were synthesized by mixing 250 mL of 1.2 M $Ca(NO_3)_2$ solution and 250 mL of 0.72 M Na_2HPO_4 solution containing appropriate stoichiometric ratios of NaF. Both $Ca(NO_3)_2$ and Na_2HPO_4/NaF solutions were dispensed at a rate of 2.4 mL/min into a 12 L reaction flask containing 10 L of deionized water that was heated to a pre-selected isothermal temperature of 95 °C. Post-synthesis, slurries were filtered and washed with 20 L of deionized water to remove salt by-products. After drying the filtered-slurry in a vacuum oven at 70 °C for 72 h, apatite powders were characterized using inductively coupled plasma mass spectrometry (ICP-MS) to determine the phosphate and calcium contents, x-ray diffraction to quantify the crystallinities, and fluoride probe to determine the fluoride content. These characterization methods were fully described in our previous manuscript (Bennett et al., 2019).

2.2. Freeze-casting process

To fabricate the freeze-cast FHA scaffolds, aqueous slurries were made with 10 vol% FHA powder mixed with 1 wt% polyvinyl alcohol of 88,000–97,000 g/mol (Alfa Aesar, Ward Hill, MA, USA) and 1 wt% polyethylene glycol of 10,000 g/mol (Alfa Aesar, Ward Hill, MA, USA) as binders, 1 wt% Dynol 604 (Evonik Industries, Essen, Germany) as a dispersant, 5 vol% of 97 % isopropyl alcohol (Sigma-Aldrich, St. Louis, MO, USA) to produce a larger pore size (Miller et al., 2018; Naleway et al., 2016), and distilled water. Individual slurries of 10 mL were sealed in a 40 mL plastic bag and sonicated at 42 kHz for 30 min to create a colloid. Sonication has been previously proven effective to homogenize freeze-cast slurries (Nelson et al., 2019a, 2019b, 2020; Silva et al., 2015; Souza et al., 2014). Immediately following sonication, the individual slurries were poured into a 20 mm diameter PVC freeze-cast mold and directionally frozen starting at room temperature at a rate of −10 °C/min in a custom freeze casting setup as previously described (Nelson et al., 2020). Slurries were then freeze-dried at 0.047 mBar and −51 °C for 96 h to fully sublimate the ice. Next, the resultant green bodies were sintered in air for 3 h at three different temperatures: 1250 °C, 1350 °C, and 1450 °C with a heating and cooling rate of 2 °C/min Starting and finishing at room temperature. The resultant products were 5 porous, freeze-cast FHA scaffolds at each sintering temperature measuring 14 mm in diameter and 20 mm in height.

2.3. Sample preparation

The freeze-cast FHA scaffolds were cut into smaller sections for testing (Fig. 1). The top and bottom sections in the lamellar region were prepared for imaging under scanning electron microscopy (SEM; FEI Quanta 600 FG, Hillsboro, OR, USA) with a 4 nm spot size and 20 kV accelerating voltage. The imaged surfaces were taken 4 mm from the top to avoid surface effects and 6 mm from the bottom to avoid the dense region that is caused by the initial rapid ice growth during freeze casting (Nelson et al., 2019b) (Fig. 1a). The remaining middle section was bisected into two discs with each being 5 mm thick (Fig. 1a). Compression samples 5 mm in height and 6 mm in radius were prepared for mechanical testing by cutting one of the discs into quarter circles (Fig. 1b). Note the smaller radius compared to the diameter of the disc was because of the removal of material when preparing the compression samples. For cell culture experiments, scaffolds (Fig. 1c) were cleaned by
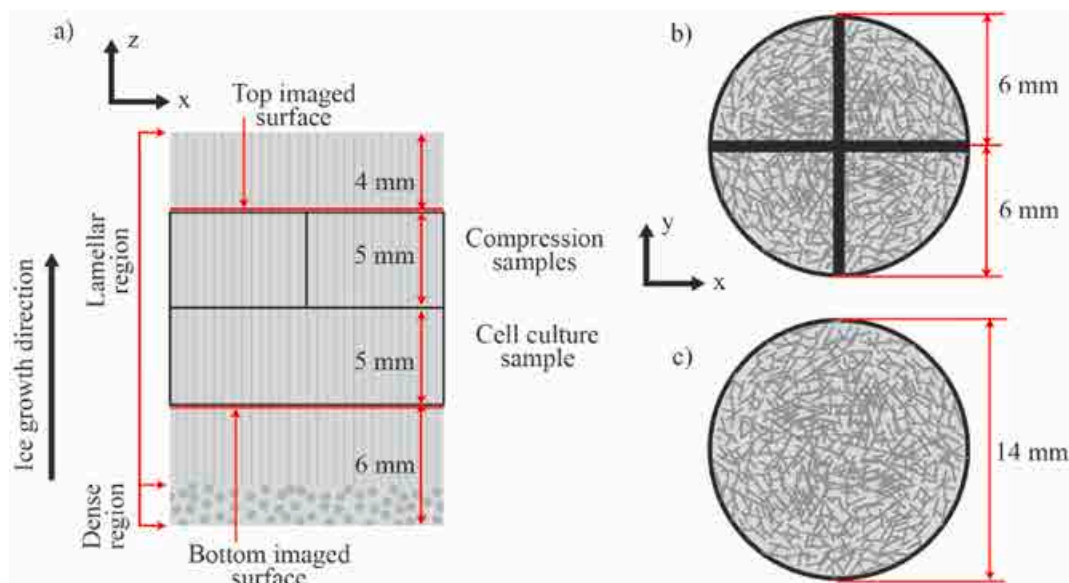
Fig. 1. An illustrated cut of a freeze-cast scaffold in the (a) x-z-plane, (b) the compression samples in the x-y-plane, (c) the cell culture sample in the x-y-plane. The lower and upper imaged surfaces were taken ≈6 mm from the bottom and ≈4 mm from the top, respectively. The cell culturing and compression samples were taken from the middle 10 mm of the scaffold. All samples and surfaces analyzed were in the lamellar section away from the initial dense section of the FHA freeze-cast scaffold. The ice growth direction is indicated along the length of the scaffold in (a). In (b) and (c), the ice growth direction is perpendicular to the page.

washing with 70 % ethanol for 2 h and sterilized using an autoclave. At each sintering temperature, the freeze-cast FHA scaffolds were prepared into 5 top imaged surfaces, 5 bottom imaged surfaces, 20 compression samples, and 5 cell culture samples. As described previously (Bennett et al., 2019), solid FHA discs were also prepared and sintered at 1250 °C to be used as cell culture controls. These discs were 11 mm in diameter and 3 mm in height and were chosen as they have been used as controls in our previous research (Bennett et al., 2019).

2.4. Material characterization

To determine the crystallographic changes from the sintering process, powder X-ray diffraction (XRD) of FHA samples before and after sintering was performed using a Miniflex 600 diffractometer (Rigaku Corporation, Tokyo, Japan). The sintered powders were prepared from crushed freeze-cast FHA scaffolds. Scans were run over a range of 10–70 °2θ at a rate of 0.5 °2θ min^{-1} with a step size of 0.05 °2θ. This resulted in four scans performed before sintering and four scans each performed after sintering at 1250 °C, 1350 °C, and 1450 °C, which resulted in a total of 16 scans.

2.5. Microstructural characterization

The microstructure of the freeze-cast FHA scaffolds in the x-y-plane (Fig. 1) was imaged using SEM (FEI Quanta 600 FG, Hillsboro, OR, USA). For this, SEM samples were coated with a 15 nm layer of gold-palladium prior to imaging. Five images of each SEM sample were taken in different areas of the scaffold. Forty images of scaffolds in the x-y-plane at each sintering temperature were analyzed using Image-J and the DiameterJ plugin (Hotaling et al., 2015) to determine the porosity, equivalent pore diameter, wall thickness, and wall porosity. The porosity was measured as the percent area that was occupied by pores versus the FHA walls (N = 40). Equivalent pore diameter was evaluated from N = 1200 samples using the ratio of perimeter to the area as used for equivalent diameters for elliptical ducts (Eq. (1)). Wall thickness was measured from N = 1200 samples as the average width of the FHA walls along their lengths. Wall porosity was measured as the percent area that was occupied by pores within the FHA walls versus the total area of the FHA walls (N = 40).

$$d_e = 1.55A^{0.625}/P^{0.25} \qquad \text{(Eq 1)}$$

where d_e is the equivalent diameter, A is the area of the pore, and p is the perimeter of the pore. In addition, the raw FHA powder was imaged using SEM after synthesis with the length and width of the powder measured with N = 40 samples each.

2.6. Mechanical testing

To determine the mechanical properties of the freeze-cast FHA scaffolds as a function of the sintering temperature, compression testing was performed using an Instron Model 5967 (Instron, Norwood, MA, USA) load frame with a 30 kN load cell. Compression test samples (n = 19/each sintering temperature) were compressed at a constant crosshead speed of 1 mm/min in the z-direction. The ultimate compressive strength and modulus of elasticity were calculated from the maximum stress and initial linear slope of the stress-strain curves, respectively.

2.7. In vitro cell culturing

Human osteoblast (hOB) cells were obtained from American Type Culture Collection (ATCC, Manassas, VA, USA). The cells were cultured in a complete medium of Dulbecco's Modified Eagle Medium (DMEM) supplemented with 10 % fetal bovine serum and 0.3 mg/mL Geneticin-418 for four days. The cell culture samples and controls were autoclaved at 250 °C for 20 min prior to seeding with 60,000 hOB cells in 200 μL of complete medium. Seeded cell culture samples and controls were incubated for a 2-h period to allow cell attachment. After the cell attachment period, the cell culture samples and controls were transferred to a 12-well plate and submerged in 2 mL of complete medium. Cells were incubated on the samples and controls for seven days. All cell culturing was maintained at 34 °C with 5 % CO_2, and the medium was changed every 2 days throughout the incubation period.

2.8. Cell viability through MTT assay

An MTT assay was performed using the Abcam MTT (tetrazolium salt) assay kit (ab211091, Burlingame, CA, USA). After a seven-day

incubation period, cell culture samples and cell culture controls were placed in 400 μL of medium consisting of a 1:1 ratio of serum-free DMEM and the MTT reagent and incubated for 3 h. After the incubation, the cell culture samples and controls were rinsed in 1x phosphate-buffered solution (PBS) and blotted dry before pictures were taken to visually observe the presence of insoluble purple formazan that occurs as a product of viable cells through mitochondrial reduction of MTT. The cell culture samples and controls were cut along the x-y plane using a razor blade to examine the presence of formazan within the interior of the scaffold. After imaging, the formazan was dissolved with 1.5 mL of MTT solvent from the assay kit. The resulting optical density was measured using a spectrophotometer (SpectraMax M3, Molecular Devices, San Jose, CA, USA) at 590 nm in accordance with the Abcam MTT assay protocol (MTT assay protocol | Abcam). Optical density readings were performed in triplicate with 5 wells containing the formazan and solvent for each scaffold in a 96-well plate for a total of 45 measurements per sintering temperature.

2.9. Statistical analysis

Analyses of variance (ANOVAs) were performed on the mechanical properties, wall thickness, wall porosity, and formazan optical density of the scaffolds between sintering temperatures using a significance of $\alpha = 0.05$. The pore size variance was determined through Levene's test of equal variance ($\alpha = 0.05$), and because of unequal variance, a Kruskal-Wallis test, the non-parametric equivalent to ANOVA, was performed ($\alpha = 0.05$). Following a result of a significant difference, a pair-wise comparison using Tukey's honest significant difference (HSD) was performed to determine which groups differed from one another, using a significance level of $\alpha = 0.05$.

3. Results and discussion

3.1. Chemical composition

Fig. 2 shows XRD data for FHA in an unsintered state and sintered at 1250 °C, 1350 °C, and 1450 °C along with the HA reference pattern. The peak shifts observed compared to the HA reference pattern reflect the change in lattice parameters of the apatite structures resulting from fluoride incorporation (Joseph Nathanael et al., 2013). FHA sintered at 1250 °C and 1350 °C showed a narrowing of peaks compared to the as-made FHA, indicating an increase in crystallinity with sintering temperature up to temperatures of 1350 °C (Chen and Miao, 2005).

Sintered ceramics have also been demonstrated to narrow the peak widths from the as-made powder, which has been attributed to poor crystallinity, nanocrystalline size, or a change in density (Fu et al., 2008b; Chen and Miao, 2005; Lebrun et al., 2016). A combination of peak broadening or amorphous humps appeared more prevalent for FHA sintered at 1450 °C, indicating a phase-change event. Peak broadening was attributed to small crystallite size, while amorphous structures might have been present due to phase decomposition into β-tricalcium phosphate (β-TCP) (Elghazel et al., 2017) (ICDD- 01-086-1585). The presence of β-TCP in FHA, when sintered above 1400 °C, has been previously observed (Chen and Miao, 2005; Elghazel et al., 2017; Taktak et al., 2018). These authors postulated that either a) an increase in the decomposition of apatite to β-TCP at high temperatures or b) a derivative formed as the result of high-temperature sintering of α-tricalcium phosphate (α-TCP) was the mechanism (Chen and Miao, 2005; Elghazel et al., 2017; Taktak et al., 2018). Composites of β-TCP and FHA have been studied and found to be favorable for bone growth, with the incorporation of FHA reducing the dissolution rate (Elghazel et al., 2017; Taktak et al., 2018).

While HA decomposition into tetracalcium phosphate (TTCP) above 1100 °C (Ou et al., 2013; Chen and Miao, 2005) and α-TCP above 1200 °C (Chen and Miao, 2005) is common, neither material was detected via XRD in sintered FHA. Both α-TCP and TTCP are associated with reduced strength and increased resorption in HA-based scaffolds (Ou et al., 2013; Chen and Miao, 2005), so no detectable presence in the sintered FHA indicated better chemical stability than is seen in HA. The observed peak broadening and phase decomposition also appeared to lead to the realignment of grain boundaries at higher sintering temperatures, which led to increased densification and strength when sintered (Chen et al., 2015; Chen and Miao, 2005). Overall, the XRD analysis corroborated the increased thermal and chemical stability provided through the partial fluoridation of hydroxyapatite into FHA and demonstrated that these advantages were maintained when the FHA was processed into freeze-cast FHA scaffolds.

3.2. Microstructure (SEM)

The unsintered FHA powder had a needle-like shape with a length much greater than the width (Fig. 3). The length and width of the powder were 990 nm ± 610 nm and 134 nm ± 47 nm, respectively. While the unique shape of the powder would alter the freezing dynamics established by Deville (2013), the use of long-chain additives PEG and PVA were employed to ensure stable scaffolds could be fabricated.
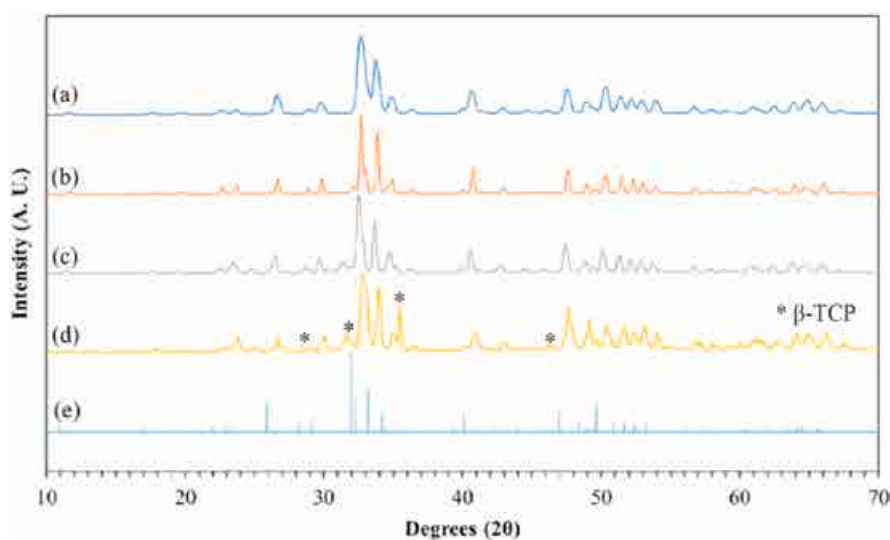

Fig. 2. XRD spectra of fluorohydroxyapatite sintered at different temperatures. (a) as-made FHA powder, (b) FHA sintered at 1250 °C, (c) FHA sintered at 1350 °C, (d) FHA sintered at 1450 °C, (e) HA reference pattern. * indicate β-TCP (ICDD- 01-086-1585).
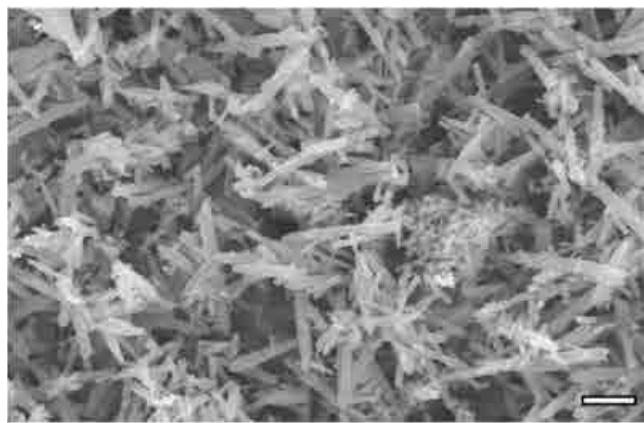
Fig. 3. SEM image of as-made FHA powder. The scale bar is 1 μm.

The observed microstructures of the freeze-cast FHA scaffolds in the x-y plane are shown in Fig. 4. To ensure blood perfusion into the scaffold structure for ideal bone regeneration, an open porosity is necessary for the transportation of nutrients, oxygen, and growth factors for the cells (Polo-Corrales et al., 2014). The open-pore microstructure of the freeze-cast FHA scaffolds matched previous studies on freeze casting with HA (Zamanian et al., 2013; Deville et al., 2006a; Fu et al., 2008b), with lamellar pores and walls appearing throughout the scaffolds. The porosity and wall thickness are listed in Table 1. The porosity was similar for the scaffolds at all three sintering temperatures (41.9 % ± 4.3 % at 1250 °C, 39.4 % ± 7.3 % at 1350 °C, 42.1 % ± 5.5 % at 1450 °C) with no statistically significant differences between sintering temperatures (p = .072).

Fig. 5 shows the mean ± standard deviation equivalent pore diameter at all three sintering temperatures as well as the probability density of the pores. Larger pores were found in 1250 °C scaffolds (with the mean equivalent pore diameter = 23.9 μm ± 14 μm) versus the 1350 °C

Table 1
Microstructural properties. Data is displayed as the mean ± the standard deviation of N = 30 measurements.

Sintering temperature [°C]	Porosity [%]	Wall thickness [μm]
1250	41.9 ± 4.3	10.6 ± 1.0
1350	39.4 ± 7.3	10.8 ± 1.5
1450	42.1 ± 5.5	9.8 ± 1.5

and 1450 °C scaffolds, which had similarly sized pore sizes (mean equivalent pore diameters of 18.5 μm ± 8.0 μm and 17.9 μm ± 7.6 μm, respectively). There were statistically significant differences in pore size when comparing the 1250 °C to 1350 °C (p = .017) and to 1450 °C (p = .003), though no statistically significant differences were found when comparing 1350 °C to 1450 °C (p = .137). The small pore size in all freeze-cast FHA scaffolds was attributed to a relatively fast cooling rate (10 °C/min) (Deville et al., 2006a), with a slower cooling rate producing larger pores. The measured equivalent diameter was comparable to pore sizes measured in previously reported freeze-cast HA scaffolds (Deville, 2010; Deville et al., 2006a; Fu et al., 2008c). Ideal pore sizes are re-ported to be at least 100 μm for bone growth (Iviglia et al., 2019; Abbasi et al., 2020), but studies using HA scaffolds have documented bone growth when using pore sizes below 50 μm both *in vivo* (Fisher et al., 2002; Roy et al., 2003) and *in vitro* (Tsuruga et al., 1997; Akay et al., 2004). Coupled with the high interconnectivity and open porosity, the scaffolds fabricated in this study are a promising alternative to bone substitutes.

Wall thickness (Table 1) did not display statistically significant dif-ferences between sintering temperatures (p = .450), with the wall thickness averaging 9 to 10 μm at all sintering temperatures. The walls of the fabricated scaffolds fell within the previously measured lamellar thickness in the cortical bone at 9.0 μm ± 2.13 μm (Pazzaglia et al., 2012). When examining the walls of the scaffolds at higher magnifica-tion (Fig. 4d–f), micro-pores were found in the walls. These wall pores have also been found in previously reported freeze-cast HA scaffolds as well (Deville et al., 2006a). Fewer wall pores were observed at higher
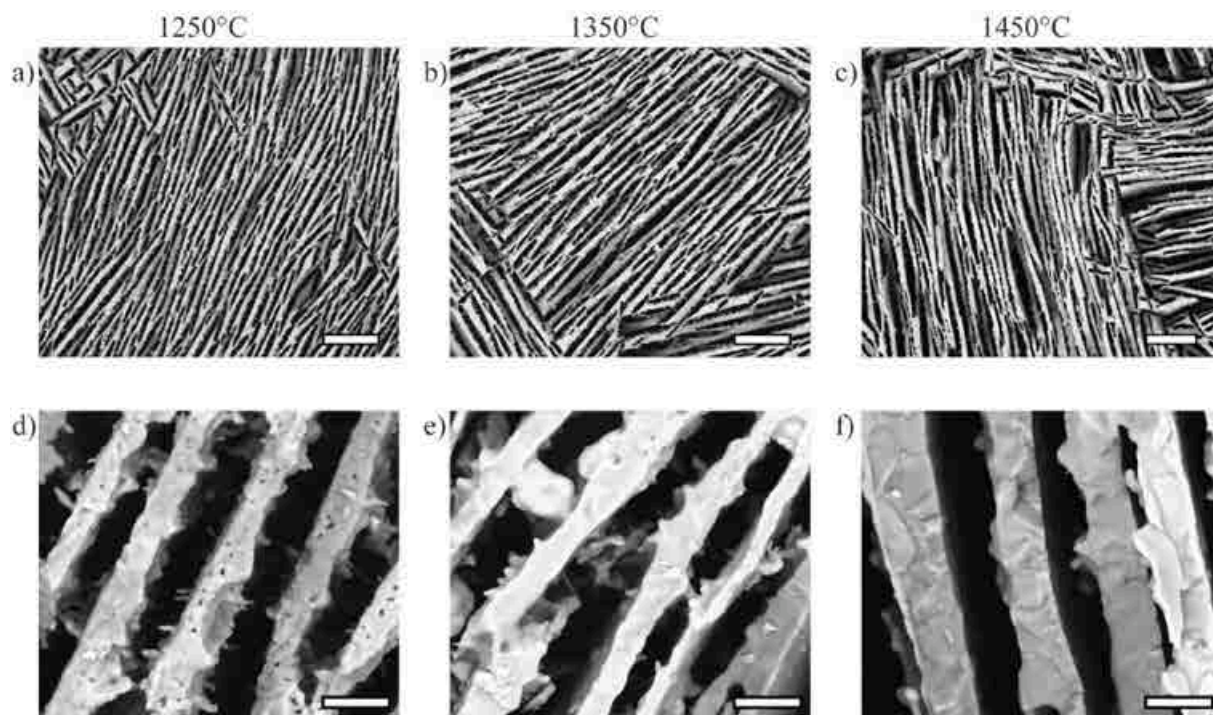

Fig. 4. SEM imaged surfaces used for measuring porosity, pore size, and wall thickness of the x-y-cross sections for: (a, d) 1250 °C, (b, e) 1350 °C, and (c, f) 1450 °C scaffolds used to measure the porosity and pore size. a–c: images taken at a lower magnification. The scale bars are 150 μm. d–f: images taken at a higher magnification shower the differences in wall structure and porosity. The scale bars are 15 μm.
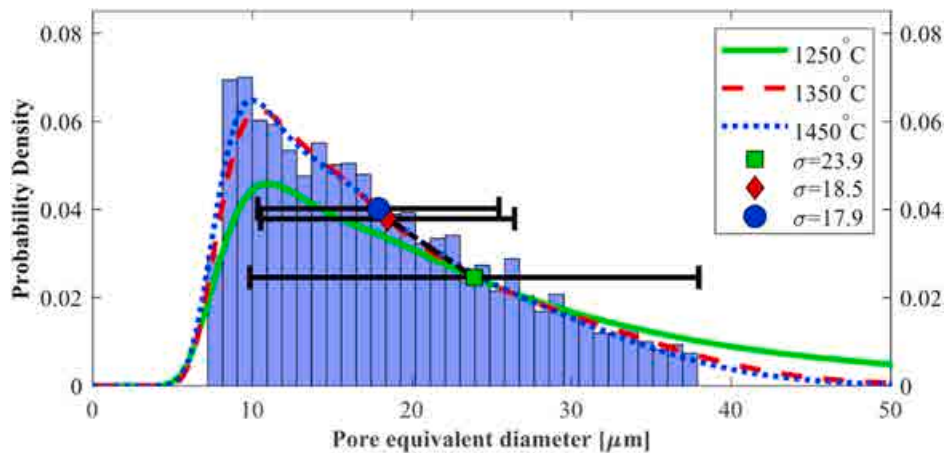
Fig. 5. Probability density distributions of N = 1200 measurements of pore size by using equivalent diameter and distinguished by sintering temperature. The histogram shows the actual probability density of pore size at 1450 °C. Means ± standard deviations of the distributions are shown through symbols and horizontal error bars: green square for 1250 °C, red diamond for 1350 °C, and blue circle for 1450 °C.

sintering temperatures leading to the conclusion that the material was not fully sintered at 1250 °C. These micropores have been reported as beneficial for cell attachment from the increased surface area (Bignon et al., 2003). The differences in wall porosity were found to be statistically significant (Fig. 6 when comparing 1250 °C to 1350 °C (p = 3.61 × 10^{-7}) and to 1450 °C (p = 7.81 × 10^{-4}). There were no statistically significant differences in wall porosity between 1350 °C and 1450 °C (p = .149). Grain size and surface roughness did not change with sintering temperatures, and therefore, it would unlikely affect the mechanical behavior and cellular response. A similar observation has been reported by Eslami et al. (2009), where they saw little to no change in grain sizes.

3.3. Mechanical behavior

Fig. 7 shows the mechanical response of the freeze-cast FHA scaffolds to compression in the z-direction, represented as the mean ± the standard deviation. With increasing sintering temperature, both the compressive strength and elastic modulus increased with the highest values at 1450 °C (13.5 MPa ± 4.0 MPa and 379 MPa ± 182 MPa, respectively). When comparing the compressive strength between sintering temperatures, statistically significant differences were found between all groups (p ≤ .032). When comparing the elastic moduli between sintering temperatures, statistically significant differences were found between 1250 °C and 1450 °C (p = 1.31 × 10^{-6}) and 1350 °C and 1450 °C (p = 1.21 × 10^{-4}). No statistically significant differences were

found between 1250 °C and 1350 °C (p = .078). The standard deviations for the elastic modulus (±76 MPa, ± 106 MPa, ± 182 MPa, at 1250 °C, 1350 °C, 1450 °C, respectively) increased with increasing sintering temperatures, indicating a larger spread of values, likely due to the variability in the microstructural lamellar walls. The increase in mechanical properties is indicative of the densification of the microstructure, where the wall porosity decreased with sintering temperature, and the scaffolds became fully sintered. The mechanical properties of HA-based freeze cast scaffolds were reported to plateau in compressive strength at sintering temperatures around 1325°C–1375 °C (Fu et al., 2008a; Deville et al., 2006a). For the freeze cast FHA scaffolds, full sintering occurred at 1450 °C as demonstrated by the mechanical properties and nonporous scaffold walls. Also, observed large increases in mechanical properties at high sintering temperatures had been attributed to the nonporous FHA samples (Qu and Wei, 2006). These results corroborated the observations of Chen and Miao (2005) (Chen and Miao, 2005) wherein FHA reached full sintering near 1450 °C. Chen and Miao postulated that the addition of fluorine slowed the densification rate, which would naturally lead to a higher sintering temperature requirement. The large gap in compressive strengths, as seen in Fig. 7, between 1350 °C and 1450 °C can similarly be reasoned as a difference between partial and full sintering.

When compared to HA scaffolds made through freeze casting and other techniques such as polymer replication, the freeze-cast FHA scaffolds showed comparable results. HA scaffolds made from polymer replication were reported to have a compressive strength of 1.3 MPa (Tripathi and Basu, 2012). Freeze-cast HA scaffolds were reported with compressive strengths ranging from 2 to 60 MPa and moduli ranging from 100 to 200 MPa depending on controllable parameters like solid loading, cooling rate, and porosity (Zamanian et al., 2013; Fu et al., 2008a; Kim et al., 2011; Deville et al., 2006a). When compared to the target application of human trabecular bone where compressive strength is 2–12 MPa, and the elastic modulus is 0.1–5 GPa (Fung and Fung, 1993), changing the sintering temperature in the current freeze-cast FHA scaffolds allowed for varying mechanical properties all within the limits of the mechanical properties of human trabecular bone. Freeze-cast FHA scaffolds sintered at 1250 °C were in line with the lower range of human trabecular bone, the 1350 °C scaffolds were in the middle of the range of human trabecular bone, and the 1450 °C scaffolds were in the upper range of human trabecular bone compressive strength, with the freeze-cast FHA scaffolds having compressive strengths of 4.17 MPa ± 0.80 MPa, 5.75 MPa ± 2.9 MPa, and 13.5 MPa ± 4.0 MPa, respectively. Therefore, similar to freeze-cast HA scaffolds, which demonstrate versatility in tailored mechanical properties, freeze-cast FHA scaffolds also provided the potential for tailored properties by
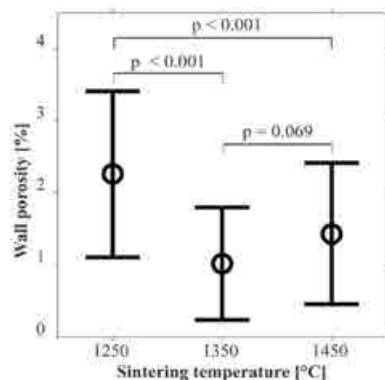

Fig. 6. Wall porosity as a function of sintering temperature. Data is displayed as the mean ± standard deviation of N = 40 measurements. Statistical significance (p < .05) between groups is noted by p-values above brackets corresponding to pairwise comparisons.
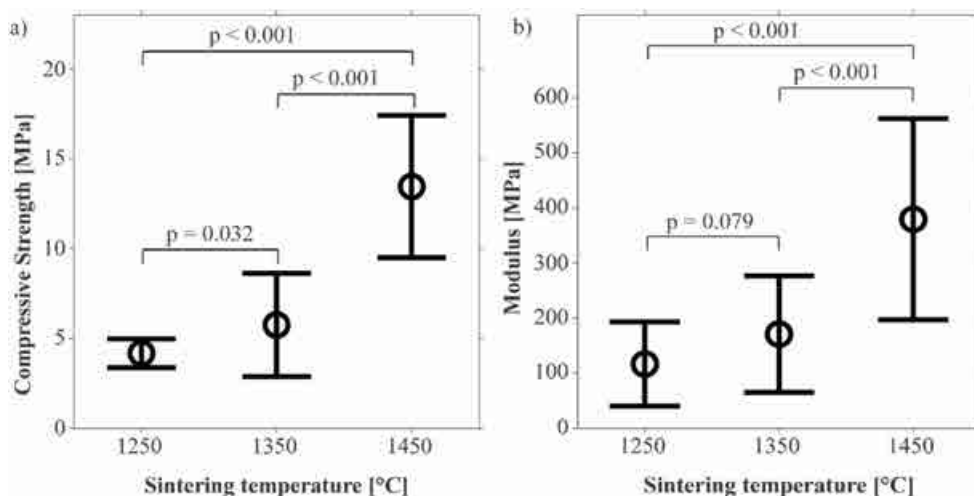
Fig. 7. Compressive strength (a) and elastic modulus (b) as a function of sintering temperature of FHA freeze-cast scaffolds. Data is displayed as the mean ± standard deviation of N = 19 measurements. Statistical significance (p < .05) between groups is noted by p-values above brackets corresponding to pairwise comparisons.

adjusting the parameters in the freeze-casting process, as demonstrated by these current results on the relationship between the mechanical properties and sintering temperature.

3.4. MTT assay

All scaffolds remained intact during the cell culturing assay, and freeze-cast FHA scaffolds seeded with hOB cells and treated with MTT at the end of incubation are shown in Fig. 8. The purple pigment visible on the scaffold was the result of mitochondrial reduction of MTT to an insoluble formazan product and signified viable cells (Fu et al., 2009a). An increase in color intensity indicated greater cell proliferation of viable cells. More formazan was produced at the top surfaces where cells were initially seeded compared to the bottom surfaces. However,

formazan produced on the bottom surface and along the interior of the scaffolds indicated the porous nature of the freeze-cast FHA scaffolds allowed for cell proliferation throughout the scaffold. This was highlighted when comparing the porous freeze-cast FHA scaffolds to a fully sintered FHA scaffold, where no formazan was observed on the bottom surface or through the interior (Fig. 8). The proliferation of cells in freeze-cast FHA scaffolds is consistent with previous studies using MTT assays on freeze-cast HA scaffolds (Fu et al., 2009a, 2009b). The penetration of formazan through the entire scaffold indicates an open porosity and interconnectivity, which is also ideal for bone regeneration as it allows for bone ingrowth and remodeling through the scaffold.

Quantitative results from the MTT assay are represented in Fig. 9 as the mean and standard deviation of the measured optical density. The cell viability showed an increase with increasing sintering temperature
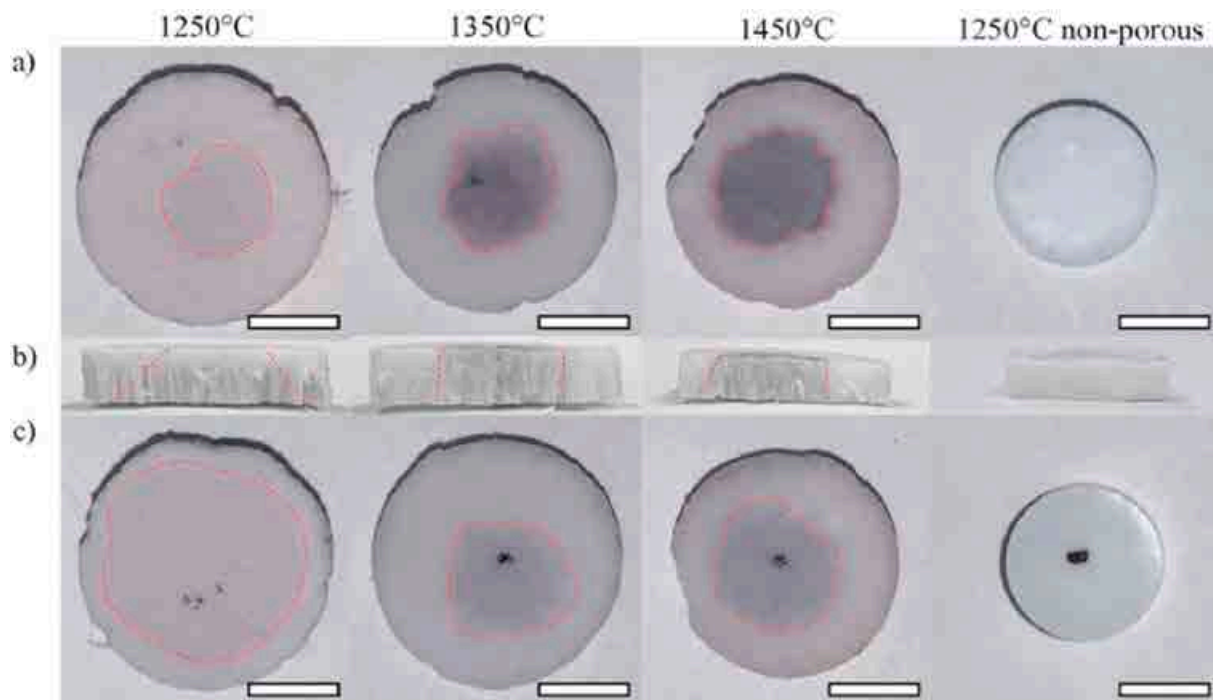

Fig. 8. Freeze-cast FHA scaffold discs sintered at varying temperatures seeded with hOB cells treated with MTT: (a) seeded surfaces in the x-y plane; (b) x-z plane cross-sections of discs showing infiltration of MTT-marked viable cells into the microstructure; (c) bottom surfaces of disks with a labeling marker to distinguish between the bottom and top surfaces. The scale bars are 5 mm.
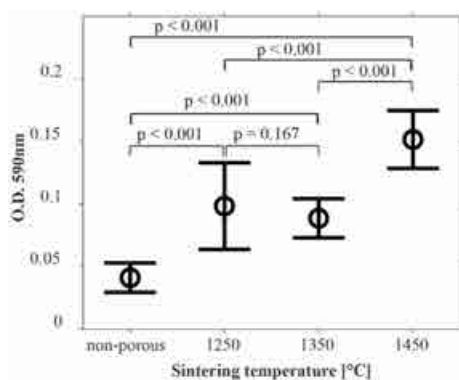
Fig. 9. Optical density (OD) of purple formazan in freeze-cast FHA scaffold discs as a function of sintering temperature along with a non-porous control. Data is displayed as the mean ± standard deviation of N = 20 measurements. Statistical significance (p < .05) between groups is noted by p-values above brackets corresponding to pairwise comparisons.

when comparing between the freeze-cast FHA scaffolds. No statistically significant differences were found when comparing 1250 °C to 1350 °C (p = .362) for cell viability. Statistically significant differences were found when comparing 1250 °C and 1350 °C to 1450 °C (p < 3.77 × 10^{-9}), with the difference attributed to the fully sintered nature of the 1450 °C scaffolds. The 1450 °C sintered scaffolds had changed chemical composition as determined from the XRD (Fig. 2) and this fully sintered nature allowed for a reduction in loose FHA particulate due to the fully sintered walls as observed through SEM (Fig. 4) and in the cell culture media. When compared to a non-porous FHA scaffold sintered at 1250 °C, the cellular response was improved for all freeze-cast FHA scaffolds with statistical significance (p < 3.77 × 10^{-9}). Due to the large surface area of the freeze-cast FHA scaffolds, cells could attain better attachment and nutrient absorption in comparison to the non-porous FHA control.

To the knowledge of the authors, this was the first time that FHA has been used to create freeze-cast scaffolds. The porosity produced by the scaffolds allowed for cell adhesion and proliferation for up to 1 week *in vitro*. When compared to porous HA scaffolds and trabecular bone, the strength was comparable, with freeze-cast FHA scaffolds sintered at 1450 °C demonstrating the greatest strength of the tested scaffolds within the upper range of trabecular bone compressive strength. As the strength and porosity are controllable through parameters in the freeze casting process, these properties could be optimized to achieve an ideal porosity with the strength to be used in load-bearing regions. Increasing the porosity would, in turn, reduce the mechanical strength, so achieving a balance between cell growth and strength would be something to pursue. Cells proliferated through all freeze-cast FHA scaffolds, with the greatest proliferation occurring in scaffolds sintered at 1450 °C. Recent studies using FHA *in vivo* and *in vitro* show improved biocompatibility compared to HA by extending implant fixation and lifespan (Rojaee et al., 2014) and limiting osteoclast differentiation to reduce bone resorption (Liu et al., 2019). Freeze-cast FHA scaffolds showed potential in applications in orthopedic and dental surgeries, however, *in vivo* bone regeneration properties need to be assessed prior to any clinical application.

4. Conclusions

The mechanical properties, material properties, and biocompatibility of freeze-cast FHA scaffolds sintered at 1250 °C, 1350 °C, and 1450 °C were evaluated. Increasing sintering temperature showed a change in the composition and structure of the FHA as well as increasing the mechanical properties. The freeze-cast FHA scaffolds showed similar pore structure and wall thickness at all sintering temperatures; however, wall pores were removed by sintering to 1450 °C, indicating fully

sintered scaffolds. Similar to the mechanical properties in human trabecular bone, a compressive strength of 13.5 ± 4.0 MPa and an elastic modulus of 379 ± 182 MPa were achieved when sintering at 1450 °C. After a 1-week incubation *in vitro*, hOB cells proliferated through all porous scaffolds, with the greatest proliferation occurring in scaffolds sintered at 1450 °C. Human osteoblast cells also migrated into the interior of the scaffolds with increasing proliferation and increasing sintering temperature. Freeze-cast FHA scaffolds showed potential to be used as osteogenic engineered bone-grafts for bone regenerative applications.

CRediT authorship contribution statement

Tony J. Yin: Data curation, Formal analysis, Investigation, Methodology, Validation, Visualization, Writing – original draft, Writing – review & editing. **Sujee Jeyapalina:** Data curation, Methodology, Supervision, Writing – review & editing. **Steven E. Naleway:** Project administration, Supervision, Writing – review & editing.

Declaration of competing interest

The authors declare that they have no known competing financial interests or personal relationships that could have appeared to influence the work reported in this paper.

Acknowledgments

References

Abbasi, N., Hamlet, S., Love, R.M., Nguyen, N.-T., 2020. Porous scaffolds for bone regeneration. J. Sci.: Adv. Matr. Dev. 5, 1–9.

Akay, G., Birch, M.A., Bokhari, M.A., 2004. Microcellular polyHIPE polymer supports osteoblast growth and bone formation in vitro. Biomaterials 25, 3991–4000.

Al-Maawi, S., Orlowska, A., Sader, R., James Kirkpatrick, C., Ghanaati, S., 2017. In vivo cellular reactions to different biomaterials—physiological and pathological aspects and their consequences. Semin. Immunol. 29, 49–61.

Alge, D.L., Cruz, G.S., Goebel, W.S., Chu, T.-M.G., 2009. Characterization of dicalcium phosphate dihydrate cements prepared using a novel hydroxyapatite-based formulation. Biomed. Mater. 4, 025016.

Arrington, E.D., Smith, W.J., Chambers, H.G., Bucknell, A.L., Davino, N.A., 1996. Ovid: complications of iliac crest bone graft harvesting. Clin. Orthop. Relat. Res. 329, 300–309.

Bai, Y., Chi, B., Ma, W., Liu, C., 2019. Suspension plasma-sprayed fluoridated hydroxyapatite coatings: effects of spraying power on microstructure, chemical stability and antibacterial activity. Surf. Coating. Technol. 361, 222–230.

Baldwin, P., et al., 2019. Autograft, allograft, and bone graft substitutes: clinical evidence and indications for use in the setting of orthopaedic trauma surgery. J. Orthop. Trauma 33, 203–213.

Belthur, M.V., Conway, J.D., Jindal, G., Ranade, A., Herzenberg, J.E., 2008. Bone graft harvest using a new intramedullary system. Clin. Orthop. Relat. Res. 466, 2973–2980.

Bennett, B.T., et al., 2019. Characterization and evaluation of fluoridated apatites for the development of infection-free percutaneous devices. Mater Sci Eng C Mater Biol Appl 100, 665–675.

Bienek, D.R., Skrtic, D., 2017. Utility of amorphous calcium phosphate-based scaffolds in dental/biomedical applications. Biointerface Res Appl Chem 7, 1989–1994.

Bignon, A., et al., 2003. Effect of micro- and macroporosity of bone substitutes on their mechanical properties and cellular response. J. Mater. Sci. Mater. Med. 14, 1089–1097.

Boyce, T., Edwards, J., Scarborough, N., 1999. Allograft bone: the influence of processing on safety and performance. Orthop. Clin. N. Am. 30, 571–581.

Chen, Y., Miao, X., 2005. Thermal and chemical stability of fluorohydroxyapatite ceramics with different fluorine contents. Biomaterials 26, 1205–1210.

Chen, J., et al., 2015. Effects of fluorine on the structure of fluorohydroxyapatite: a study by XRD, solid-state NMR and Raman spectroscopy. J. Mater. Chem. B 3, 34–38.

Chu, K.-T., et al., 2013. Research of phase transformation induced biodegradable properties on hydroxyapatite and tricalcium phosphate based bioceramic. Ceram. Int. 39, 1455–1462.

Dehghanghadikolaei, A., Fotovvati, B., 2019. Coating techniques for functional enhancement of metal implants for bone replacement: a review. Materials 12, 1795.

Deisinger, U., et al., 2008. Fabrication of tailored hydroxyapatite scaffolds: comparison between a direct and an indirect rapid prototyping technique. Key Eng. Mater. 361–363, 915–918. https://www.scientific.net/KEM.361-363.915.

Deville, S., 2010. Freeze-casting of porous biomaterials: structure, properties and opportunities. Materials 3, 1913–1927.

Deville, S., 2013. Ice-templating, freeze casting: beyond materials processing. J. Mater. Res. 28, 2202–2219.

Deville, S., Saiz, E., Tomsia, A.P., 2006a. Freeze casting of hydroxyapatite scaffolds for bone tissue engineering. Biomaterials 27, 5480–5489.

Deville, S., Saiz, E., Nalla, R.K., Tomsia, A.P., 2006b. Freezing as a path to build complex composites. Science 311, 515–518.

Deville, S., Saiz, E., Tomsia, A.P., 2007. Ice-templated porous alumina structures. Acta Mater. 55, 1965–1974.

Diez, M., Kang, M.-H., Kim, S.-M., Kim, H.-E., Song, 2016. J. Hydroxyapatite (HA)/poly-L-lactic acid (PLLA) dual coating on magnesium alloy under deformation for biomedical applications. J. Mater. Sci. Mater. Med. 27, 34.

Dutta, S.R., Passi, D., Singh, P., Bhuibhar, A., 2015. Ceramic and non-ceramic hydroxyapatite as a bone graft material: a brief review. Ir. J. Med. Sci. 184, 101–106.

Elghazel, A., Taktak, R., Bouaziz, J., Keskes, S.C., Tcp, H., 2017. Fluorapatite composite scaffolds: mechanical characterization and in vitro/in vivo testing. In: Scaffolds in Tissue Engineering - Materials, Technologies and Clinical Applications. https://doi.org/10.5772/intechopen.69852.

Eslami, H., Solati-Hashjin, M., Tahriri, M., 2009. The comparison of powder characteristics and physicochemical, mechanical and biological properties between nanostructure ceramics of hydroxyapatite and fluoridated hydroxyapatite. Mater. Sci. Eng. C 29, 1387–1398.

Fathi, M.H., Mohammadi Zahrani, E., 2009. Mechanical alloying synthesis and bioactivity evaluation of nanocrystalline fluoridated hydroxyapatite. J. Cryst. Growth 311, 1392–1403.

Fisher, J.P., et al., 2002. Soft and hard tissue response to photocrosslinked poly (propylene fumarate) scaffolds in a rabbit model. J. Biomed. Mater. Res. 59, 547–556.

Fu, Q., Rahaman, M.N., Dogan, F., Bal, B.S., 2008a. Freeze casting of porous hydroxyapatite scaffolds. II. Sintering, microstructure, and mechanical behavior. J. Biomed. Mater. Res. B Appl. Biomater. 86B, 514–522.

Fu, Q., Rahaman, M.N., Dogan, F., Bal, B.S., 2008b. Freeze casting of porous hydroxyapatite scaffolds. I. Processing and general microstructure. J. Biomed. Mater. Res. B Appl. Biomater. 86B, 125–135.

Fu, Q., Rahaman, M.N., Dogan, F., Bal, B.S., 2008c. Freeze-cast hydroxyapatite scaffolds for bone tissue engineering applications. Biomed. Mater. 3, 025005.

Fu, Q., Rahaman, M.N., Bal, B.S., Brown, R.F., 2009a. In vitro cellular response to hydroxyapatite scaffolds with oriented pore architectures. Mater. Sci. Eng. C 29, 2147–2153.

Fu, Q., Rahaman, M.N., Bal, B.S., Brown, R.F., 2009b. Proliferation and function of MC3T3-E1 cells on freeze-cast hydroxyapatite scaffolds with oriented pore architectures. J Mater. Sci. Mater. Med. 20, 1159–1165.

Fung, Y.-C., 1993. Bone and cartilage. In: Fung, Y.-C. (Ed.), Biomechanics: Mechanical Properties of Living Tissues, vols. 500–544. Springer. https://doi.org/10.1007/978-1-4757-2257-4_12.

Gaviria, L., Salcido, J.P., Guda, T., Ong, J.L., 2014. Current trends in dental implants. J Korean Assoc Oral Maxillofac Surg 40, 50–60.

Ghanaati, S., et al., 2010. Histological and histomorphometrical analysis of a silica matrix embedded nanocrystalline hydroxyapatite bone substitute using the subcutaneous implantation model in Wistar rats. Biomed. Mater. 5, 035005.

Ghanaati, S., et al., 2012. The chemical composition of synthetic bone substitutes influences tissue reactions in vivo : histological and histomorphometrical analysis of the cellular inflammatory response to hydroxyapatite, beta-tricalcium phosphate and biphasic calcium phosphate ceramics. Biomed. Mater. 7, 015005.

Ghazanfari, S.M.H., Zamanian, A., 2013. Phase transformation, microstructural and mechanical properties of hydroxyapatite/alumina nanocomposite scaffolds produced by freeze casting. Ceram. Int. 39, 9835–9844.

Habraken, W.J.E.M., Wolke, J.G.C., Jansen, J.A., 2007. Ceramic composites as matrices and scaffolds for drug delivery in tissue engineering. Adv. Drug Deliv. Rev. 59, 234–248.

Han, J., Hong, C., Zhang, X., Du, J., Zhang, W., 2010. Highly porous ZrO2 ceramics fabricated by a camphene-based freeze-casting route: microstructure and properties. J. Eur. Ceram. Soc. 30, 53–60.

Hench, L.L., 1998. Bioceramics. *Journal of the American Ceramic Society* 81, 1705–1728.

Hotaling, N.A., Bharti, K., Kriel, H., Simon, C.G., 2015. DiameterJ: a validated open source nanofiber diameter measurement tool. Biomaterials 61, 327–338.

Iviglia, G., Kargozar, S., Baino, F., 2019. Biomaterials, current strategies, and novel nano-technological approaches for periodontal regeneration. J. Funct. Biomater. 10, 3.

Jo, I.-H., et al., 2009. Highly porous hydroxyapatite scaffolds with elongated pores using stretched polymeric sponges as novel template. Mater. Lett. 63, 1702–1704.

Joseph Nathanael, A., et al., 2013. Influence of fluorine substitution on the morphology and structure of hydroxyapatite nanocrystals prepared by hydrothermal method. Mater. Chem. Phys. 137, 967–976.

Kang, I.-G., Park, C.-I., Lee, H., Kim, H.-E., Lee, S.-M., 2018. Hydroxyapatite microspheres as an additive to enhance radiopacity, biocompatibility, and osteoconductivity of poly(methyl methacrylate). Bone Cement. *Materials (Basel)* 11.

Kattimani, V.S., Kondaka, S., Lingamaneni, K.P., 2016. Hydroxyapatite––Past, present, and future in bone regeneration. Bone Tissue Regen. Insights 7. BTRI.S36138.

Kim, H.-W., Kong, Y.-M., Bae, C.-J., Noh, Y.-J., Kim, H.-E., 2004. Sol–gel derived fluor-hydroxyapatite biocoatings on zirconia substrate. Biomaterials 25, 2919–2926.

Kim, M.-S., Park, I.-H., Lee, B.-T., 2009. Fabrication and characterization of porous hydroxyapatite scaffolds. Korean Journal of Materials Research 19, 680–685.

Kim, J., et al., 2011. A comparative study of the physical and mechanical properties of porous hydroxyapatite scaffolds fabricated by solid freeform fabrication and polymer replication method. Int. J. Precis. Eng. Manuf. 12, 695–701.

Lebrun, J.-M., et al., 2016. The change of X-ray diffraction peak width during in situ conventional sintering of nanoscale powders. J. Am. Ceram. Soc. 99.

Lee, E.-J., Koh, Y.-H, Yoon, B.-H., Kim, H.-E., Kim, H.-W., 2007. Highly porous hydroxyapatite bioceramics with interconnected pore channels using camphene-based freeze casting. Mater. Lett. 61, 2270–2273.

Lee, H., Jang, T.-S., Song, J., Kim, H.-E., Jung, H.-D., 2017. The production of porous hydroxyapatite scaffolds with graded porosity by sequential freeze-casting. Materials 10.

Lee, J.I., et al., 2019. Synthesis of bioinspired ice-templated bulk metallic glass-alumina composites with intertwined dendritic structure. Scripta Mater. 172, 159–164.

Liu, S., et al., 2019. Fluorine-contained hydroxyapatite suppresses bone resorption through inhibiting osteoclasts differentiation and function in vitro and in vivo. Cell Prolif 52, e12613.

Luo, Y., Li, D., Zhao, J., Yang, Z., Kang, P., 2018. In vivo evaluation of porous lithium-doped hydroxyapatite scaffolds for the treatment of bone defect. Bio Med. Mater. Eng. 29, 699–721.

Miller, S., Xiao, X., Setlock, J., Farmer, S., Faber, K., 2018. Freeze-cast yttria-stabilized zirconia pore networks: effects of alcohol additives. Int. J. Appl. Ceram. Technol. 15, 296–306.

Milovac, D., Gamboa-Martínez, T.C., Ivankovic, M., Gallego Ferrer, G., Ivankovic, H., 2014. PCL-coated hydroxyapatite scaffold derived from cuttlefish bone: in vitro cell culture studies. Mater. Sci. Eng. C 42, 264–272.

Munch, E., et al., 2008. Porous ceramic scaffolds with complex architectures. J. Occup. Med. 60, 54–58.

Munch, E., Saiz, E., Tomsia, A.P., Deville, S., 2009. Architectural control of freeze-cast ceramics through additives and templating. J. Am. Ceram. Soc. 92, 1534–1539.

Naleway, S.E., et al., 2016. Bioinspired intrinsic control of freeze cast composites: harnessing hydrophobic hydration and clathrate hydrates. Acta Mater. 114, 67–79.

Nelson, I., Gardner, L., Carlson, K., Naleway, S.E., 2019a. Freeze casting of iron oxide subject to a tri-axial nested Helmholtz-coils driven uniform magnetic field for tailored porous scaffolds. Acta Mater. 173, 106–116.

Nelson, I., et al., 2019b. Freeze-casting of surface-magnetized iron(II,III) oxide particles in a uniform static magnetic field generated by a helmholtz coil. Adv. Eng. Mater. 21, 1801092.

Nelson, I., et al., 2020. Helical and bouligand porous scaffolds fabricated by dynamic low strength magnetic field freeze casting. J. Occup. Med. 72, 1498–1508.

Nuss, K.M.R., von Rechenberg, B., 2008. Biocompatibility issues with modern implants in bone - a review for clinical orthopedics. Open Orthop. J. 2, 66–78.

Ou, S.-F., Chiou, S.-Y., Ou, K.-L., 2013. Phase transformation on hydroxyapatite decomposition. Ceram. Int. 39, 3809–3816.

Pazzaglia, U.E., Congiu, T., Marchese, M., Spagnuolo, F., Quacci, D., 2012. Morphometry and patterns of lamellar bone in human haversian systems. Anat. Rec. 295, 1421–1429.

Polo-Corrales, L., Latorre-Esteves, M., Ramirez-Vick, 2014. J. E. Scaffold design for bone regeneration. J. Nanosci. Nanotechnol. 14, 15–56.

Qu, H., Wei, M., 2006. Effect of fluorine content on mechanical properties of sintered fluoridated hydroxyapatite. Mater. Sci. Eng. C 26, 46–53.

Rabiee, S.M., Moztarzadeh, F., Solati-Hashjin, M., 2010. Synthesis and characterization of hydroxyapatite cement. J. Mol. Struct. 969, 172–175.

Ramay, H.R.R., Zhang, M., 2004. Biphasic calcium phosphate nanocomposite porous scaffolds for load-bearing bone tissue engineering. Biomaterials 25, 5171–5180.

Rojaee, R., Fathi, M., Raeissi, K., Sharifnabi, A., 2014. Biodegradation assessment of nanostructured fluoridated hydroxyapatite coatings on biomedical grade magnesium alloy. Ceram. Int. 40, 15149–15158.

Roy, T.D., et al., 2003. Performance of degradable composite bone repair products made via three-dimensional fabrication techniques. J. Biomed. Mater. Res. 66, 283–291.

Russell, J.L., Block, J.E., 2000. Surgical harvesting of bone graft from the ilium: point of view. Med. Hypotheses 55, 474–479.

Silva, A.M.A., et al., 2015. Effect of titania addition on the properties of freeze-cast alumina samples. Ceram. Int. 41, 10467–10475.

Sopyan, I., Gunawan, 2013. Development of porous calcium phosphate bioceramics for bone implant applications: a review. MATS 6, 238–252.

Souza, D.F., et al., 2014. Synthesis and structural evaluation of freeze-cast porous alumina. Mater. Char. 96, 183–195.

MTT assay protocol | Abcam. https://www.abcam.com/kits/mtt-assay-protocol.

Taktak, R., Elghazal, A., Bouaziz, J., Charfi, S., Keskes, H., 2018. Tricalcium phosphate-Fluorapatite as bone tissue engineering: evaluation of bioactivity and biocompatibility. Mater. Sci. Eng. C 86, 121–128.

Tang, Y., Qiu, S., Wu, C., Miao, Q., Zhao, K., 2016. Freeze cast fabrication of porous ceramics using tert-butyl alcohol–water crystals as template. J. Eur. Ceram. Soc. 36, 1513–1518.

Thrivikraman, G., Athirasala, A., Twohig, C., Boda, S.K., Bertassoni, L.E., 2017. Biomaterials for craniofacial bone regeneration. Dent. Clin. 61, 835–856.

Tripathi, G., Basu, B., 2012. A porous hydroxyapatite scaffold for bone tissue engineering: physico-mechanical and biological evaluations. Ceram. Int. 38, 341–349.

Tsuruga, E., Takita, H., Itoh, H., Wakisaka, Y., Kuboki, Y., 1997. Pore size of porous hydroxyapatite as the cell-substratum controls BMP-induced osteogenesis. J. Biochem. 121, 317–324.

Tuchman, A., et al., 2016. Iliac crest bone graft versus local autograft or allograft for lumbar spinal fusion: a systematic review. Global Spine J. 6, 592–606.

van de Vijfeijken, S.E.C.M., et al., 2018. Autologous bone is inferior to alloplastic cranioplasties: safety of autograft and allograft materials for cranioplasties, a systematic review. World Neurosurgery 117, 443–452 e8.

Wilson, C.E., Bruijn, J. D. de, Blitterswijk, C. A. van, Verbout, A.J., Dhert, W.J.A., 2004. Design and fabrication of standardized hydroxyapatite scaffolds with a defined macro-architecture by rapid prototyping for bone-tissue-engineering research. J. Biomed. Mater. Res. 68A, 123–132.

Yook, S.-W., et al., 2012. Reverse freeze casting: a new method for fabricating highly porous titanium scaffolds with aligned large pores. Acta Biomater. 8, 2401–2410.

Zamanian, A., Farhangdoust, S., Yasaei, M., Khorami, M., Abbasabadi, M., 2013. The effect of sintering temperature on the microstructural and mechanical characteristics of hydroxyapatite macroporous scaffolds prepared via freeze-casting. Key Eng. Mater. https://www.scientific.net/KEM.529-530.133.

Zhao, H., et al., 2010. The formation mechanism of the β-TCP phase in synthetic fluorohydroxyapatite with different fluorine contents. Biomed. Mater. 5, 045011.